

A hybrid smoothed extended finite element/level set method for modeling equilibrium shapes of nano-inhomogeneities

Xujun Zhao¹, Stéphane P.A. Bordas³ and Jianmin Qu^{1,2}

¹Department of Mechanical Engineering, Northwestern University, Evanston, IL USA 60208

²Department of Civil and Environmental Engineering, Northwestern University, Evanston, IL USA 60208

³Cardiff School of Engineering, Institute of Mechanics and Advanced Materials Theoretical, Applied and Computational Mechanics, Cardiff University, The Parade, Cardiff CF24 3AA, Wales, U.K.

E-mail: j-qu@northwestern.edu, stephane.bordas@alum.northwestern.edu.

Abstract

Interfacial energy plays an important role in equilibrium morphologies of nanosized microstructures of solid materials due to the high interface-to-volume ratio, and can no longer be neglected as it does in conventional mechanics analysis. The present work develops an effective numerical approach by means of a hybrid smoothed extended finite element/level set method to model nanoscale inhomogeneities with interfacial energy effect, in which the finite element mesh can be completely independent of the interface geometry. The Gurtin-Murdoch surface elasticity model is used to account for the interface stress effect and the Wachspres interpolants are used for the first time to construct the shape functions in the smoothed extended finite element method. Selected numerical results are presented to study the accuracy and efficiency of the proposed method as well as the equilibrium shapes of misfit particles in elastic solids. The presented results compare very well with those obtained from theoretical solutions and experimental observations, and the computational efficiency of the method is shown to be superior to that of its most advanced competitor.

Keywords: Smoothed extended finite element method; Level set method; Wachspres shape function; Interface excess energy; Equilibrium shape.

1. Introduction

Recent advances in nanotechnology exacerbate the need for computational tools that are capable of capturing the effects of interfaces, which play an important role in nanostructured materials due to a characteristically high interface-to-volume ratio. Although atomic level computational tools such as molecular dynamic (MD) and first principle calculations are able to simulate interface effects, these methods are computationally intensive, thus their applications are usually limited to nano-scale samples and nano-second time durations. Many engineering problems, however, occur at much larger spatial and temporal scales. For example, simulating the formation and morphological evolution of precipitates in superalloys involves length scales ranging from several nanometers to tens of micrometers, and the physical processes last up to hours in time. In these cases, it is necessary to use a continuum level model that can capture the interfacial effects of particles at different length and time scales.

The bonding environment of atoms near surfaces/interfaces differs from that in the bulk, so that the energy associated with surfaces/interfaces is also different from the bulk energy. This

effect will be prominent for nanostructured materials when the surface-to-volume ratio is high. Gurtin and Murdoch [1, 2] developed a generic continuum model incorporating the surface/interface effects where the surface/interface is modeled as a zero-thickness layer with its own physical properties. This surface/interface elasticity model has been extensively used to model nanostructures [3-8], and it was shown that the size-dependent behaviors obtained from the surface elasticity model agree very well with the atomistic simulations [4, 9].

However, these theoretical results are limited to systems with either simple geometries or isotropic material properties. To characterize the size dependent behavior of nanosized structures with more realistic geometries and anisotropic properties, standard finite element methods (FEM) incorporating surface/interface effects were developed by introducing surface/interface elements [10-15]. In addition, Park and coworkers [16-18] developed a Cauchy-Born model for nanoscale material analysis, in which surface energies are obtained directly from an underlying crystal structure and interatomic potential. Within the standard FEM framework, it is required that both the bulk mesh and the interface mesh conform to the material interface in order to describe the strain discontinuities across the interface, so that remeshing is generally required when the interface moves. This usually leads to difficulties for inhomogeneities with very complex and evolving geometries, especially when the inhomogeneities are numerous and evolving with time.

The extended finite element method (XFEM), which was originally developed to model cracks in fracture mechanics [19], is a robust and powerful computational tool capable of modeling arbitrary discontinuities without requiring the meshes to be conformed with the discontinuity interfaces. The XFEM has been successfully used to solve many physical problems with arbitrary interfaces, such as holes and inclusions [20], phase solidification [21], multiphase flows [22], biofilm growth [23, 24], etc. A comprehensive review of XFEM can be found in [25] and an open source C++ XFEM code is also available for use [26]. Recently, Yvonnet et al. [27] developed an XFEM/level set approach to study the size-dependent effective properties of nanocomposites based on a Gurtin-Murdoch model with the coherent interface assumption [1]. Moreover, Farsad et al. [28] presented an XFEM approach allowing for strong discontinuities across the interface based on a Gurtin-Murdoch incoherent interface model [2] and they studied the surface/interface effects on the mechanical behaviors of nanoscale materials. However, they limited their studies to static models without considering the evolution of the interfaces.

In this paper, we developed a hybrid smoothed extended finite element/level set method incorporating the interfacial energy effect, in which a level set function is used to implicitly capture the motion of the interface and the finite element mesh is independent of the interface geometry, so that no remeshing is required even when the interfaces move, merge, cusp or disappear. The strain smoothing technique [29] is applied to modify the standard XFEM so that the domain integrals in each element can be transformed into contour integrals along the boundaries of smoothing cells. Such a transformation alleviates the needs of numerically evaluating the Jacobian matrix and derivatives of the shape functions, which reduces the computational cost without loss of accuracy. The Wachspress interpolants [30] are used to construct the shape functions, which greatly facilitate the numerical quadrature along the boundaries of smoothing cells. We present some numerical examples to illustrate the computational accuracy and convergence of the Smoothed XFEM, followed by an example to study the influence of interface effects on the equilibrium shape of particles with different sizes.

2. Formulation

Consider a finite elastic domain V containing multiple inhomogeneities with arbitrary shapes and misfit strain $\boldsymbol{\varepsilon}^*$ (eigenstrain). Ω is the union of all the inhomogeneities and $\Gamma = \partial\Omega$ denotes the interfaces between the inhomogeneities and the matrix. Further, we

assume that V is subjected to a prescribed body force \mathbf{b} , a surface traction \mathbf{t} on S_t and a displacement \mathbf{u}_0 on S_u , where $S = S_u \cup S_t$.

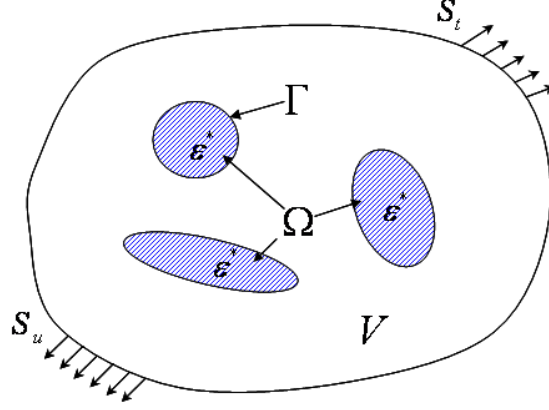


Figure 1. Inhomogeneities in a finite matrix

In terms of the displacement vector \mathbf{u} and the total strain tensor $\boldsymbol{\varepsilon}$, the total potential energy Π of the composite consists of three parts: the elastic energy U^B in the bulk, the interfacial energy U^S on all the inhomogeneity-matrix interfaces, and the work done by external forces W , i.e.,

$$\Pi = U^B + U^S + W \quad (1)$$

where

$$U^B = \frac{1}{2} \int_{V \setminus \Omega} \boldsymbol{\varepsilon} : \mathbf{L}^M : \boldsymbol{\varepsilon} \, d\Omega + \frac{1}{2} \int_{\Omega} (\boldsymbol{\varepsilon} - \boldsymbol{\varepsilon}^*) : \mathbf{L}^I : (\boldsymbol{\varepsilon} - \boldsymbol{\varepsilon}^*) \, d\Omega \quad (2)$$

$$U^S = \int_{\Gamma} \gamma \, dS \quad (3)$$

$$W = - \int_V \mathbf{u} \cdot \mathbf{b} \, d\Omega - \int_{S_t} \mathbf{u} \cdot \mathbf{t} \, dS \quad (4)$$

where γ is the interfacial excess energy density [7] given by

$$\gamma = \gamma_0 + \boldsymbol{\tau}^S : \boldsymbol{\varepsilon}^S + \frac{1}{2} \boldsymbol{\varepsilon}^S : \mathbf{L}^S : \boldsymbol{\varepsilon}^S \quad (5)$$

In the above, field quantities with a superscript I , M and S are associated with the inhomogeneity, the matrix and the interfaces, respectively. For example, \mathbf{L}^I and \mathbf{L}^M represent the elastic stiffness tensors of inhomogeneities and matrix. $\boldsymbol{\varepsilon}^S$ is the interface strain tensor, and \mathbf{L}^S is the interface elastic stiffness tensor. $\boldsymbol{\tau}^S$ is the interface residual stress and γ_0 is the interfacial excess energy density that corresponds to the interfacial energy state when $\boldsymbol{\varepsilon}^S = \mathbf{0}$. It should be mentioned that the constant γ_0 has no influence on the elastic field for a specific configuration but contributes to the total system energy.

The corresponding interfacial stress can be obtained from the Shuttleworth equation [31],

$$\boldsymbol{\sigma}^S = \frac{\partial \gamma}{\partial \boldsymbol{\varepsilon}^S} = \boldsymbol{\tau}^S + \mathbf{L}^S : \boldsymbol{\varepsilon}^S \quad (6)$$

According to the coherent interface assumption, the interfacial strain can be obtained by taking the tangential gradient of the displacement vector [1]

$$\boldsymbol{\varepsilon}^S = \frac{1}{2} \left[\nabla_s \otimes \mathbf{u} + (\nabla_s \otimes \mathbf{u})^T \right] \quad (7)$$

where $\nabla_s = \mathbf{P} \cdot \nabla$ is the interfacial gradient, $\mathbf{P} = \mathbf{I} - \mathbf{n} \otimes \mathbf{n}$ is the tangential projection

operator. Here, \mathbf{n} is the outward unit normal to the interface and \mathbf{I} is the second order identity tensor.

Under equilibrium, the system minimizes its potential energy and the stationary condition requires the variation of the functional to vanish, i.e. $\delta\Pi = 0$, which gives

$$\delta\Pi = \delta U^b + \delta U^S + \delta W = 0 \quad (8)$$

where

$$\begin{aligned} \delta U^b &= \int_{V-\Omega} \boldsymbol{\varepsilon} : \mathbf{L}^M : \delta\boldsymbol{\varepsilon} d\Omega + \int_{\Omega} (\boldsymbol{\varepsilon} - \boldsymbol{\varepsilon}^*) : \mathbf{L}^I : \delta\boldsymbol{\varepsilon} d\Omega \\ \delta U^S &= \int_{\Gamma} [\boldsymbol{\tau}^S : \delta\boldsymbol{\varepsilon}^S + \boldsymbol{\varepsilon}^S : \mathbf{L}^S : \delta\boldsymbol{\varepsilon}^S] dS \\ \delta W &= -\int_{\Omega} \mathbf{b} \cdot \delta\mathbf{u} d\Omega - \int_{S_i} \mathbf{t} \cdot \delta\mathbf{u} dS \end{aligned} \quad (9)$$

Equation (8) will be used later to develop the weak form of the finite element equations.

3. Level set description of the interfaces

The level set method was originally devised for tracking a moving interface [32], and became a key ingredient of XFEM to implicitly describe complicated geometrical interfaces of microstructures without tracking them explicitly, such as cracks [33], holes and inclusions [20, 34], dislocations [35] and biofilms [23, 24], as well as fluid-structure interfaces [36].

In this paper, the interfaces between the inhomogeneities and the matrix can be defined as the zero level set of a function $\phi(\mathbf{x})$, such that $\phi < 0$ in the particles, $\phi > 0$ in the matrix and $\phi = 0$ on the interface, which is as shown in Figure 2. Often, the signed distance is used as

$$\phi(\mathbf{x}) = \|\mathbf{x} - \mathbf{x}_{\min}\| \text{sign}(\mathbf{n}_{\min} \cdot (\mathbf{x} - \mathbf{x}_{\min})) \quad (10)$$

where \mathbf{x}_{\min} is the orthogonal projection of \mathbf{x} on the interface Γ , \mathbf{n}_{\min} is the outward unit normal at \mathbf{x}_{\min} , and $\text{sign}(\bullet)$ denotes the sign function.

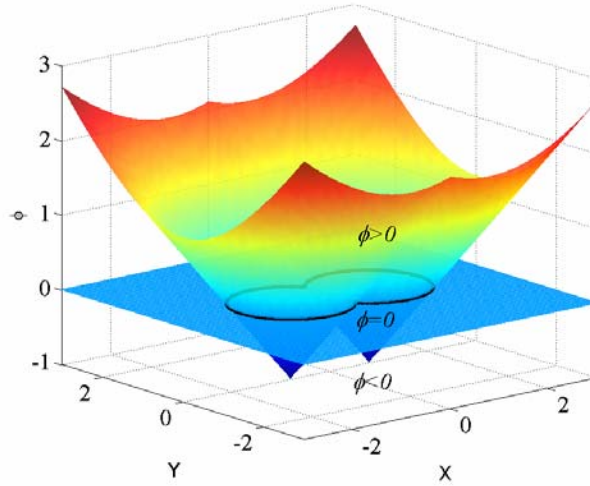


Figure 2. Level set function

It should be pointed out that the function $\phi(\mathbf{x})$ is usually not known explicitly, or analytically, except for simple shapes (circles, ellipses, etc.), but can be approximated by a set of local values, ϕ_I , at the finite element nodes:

$$\phi(\mathbf{x}) = \sum_{I=1}^M N_I(\mathbf{x}) \phi_I \quad (11)$$

where $N_I(\mathbf{x})$ is the finite element shape function of node I , and M is the total number of nodes in an element.

An initial value partial differential equation then can be obtained for the evolution of ϕ by taking a material derivative on both sides of (10) [32]

$$\frac{\partial \phi}{\partial t} + v_n^{ext} |\nabla \phi| = 0 \quad (12)$$

which is the well-known level set equation. The position of the interface at time t is defined by the zero level set $\phi(\mathbf{x}, t) = 0$. $v_n^{ext} = \mathbf{v} \cdot \mathbf{n}$ is the normal velocity on the interface

A main advantage of the level set description is its ability to describe an arbitrary number of inhomogeneities with a single level set function. The geometric quantities such as normal vector \mathbf{n} and curvature κ can be easily expressed in terms of level set function, e.g.

$$\mathbf{n} = \frac{\nabla \phi}{|\nabla \phi|}, \quad \kappa = \nabla \cdot \frac{\nabla \phi}{|\nabla \phi|} \quad (13)$$

Additionally, when the interfaces evolve in time, merge, create cusps, coalesce, the hybrid smoothed XFEM/level set method can deal with the topological transformation naturally without remeshing or other special treatments.

4. Smoothed extended finite element method

In this section, we present the basic idea of the strain smoothing technique and formulate the Smoothed XFEM (SmXFEM) to account for the effects of interfaces. This will be based on the Wachspress shape functions[30]. The implementation of boundary integration and smoothing cell subdivision will also be discussed.

4.1 Strain smoothing in finite element

The strain smoothing technique was first proposed in the context of mesh-free methods to stabilize nodal integration [37]. Liu et al. [29] introduced this method into the conventional finite element formulation. Without introducing additional degrees of freedom, an element is further subdivided into several smoothing cells, and a smoothing operation is performed in each cell within an element by a weighted average of the standard FEM strain field in the Voigt notation, $\boldsymbol{\varepsilon}^h \equiv [\varepsilon_{11}^h, \varepsilon_{22}^h, \gamma_{12}^h]^T$. We note that the Voigt notation for the strain tensors will be used in the rest of this paper, except Section 5 where the tensorial notation is used.

For example, the smoothed strain value at a point \mathbf{x}_k can be expressed as

$$\bar{\boldsymbol{\varepsilon}}(\mathbf{x}_k) = \int_{\Omega_k^s} \boldsymbol{\varepsilon}^h(\mathbf{x}) W(\mathbf{x}_k - \mathbf{x}) d\Omega \quad (14)$$

where Ω_k^s is the smoothing cell defined in the local vicinity of \mathbf{x}_k and $W(\mathbf{x}_k - \mathbf{x})$ is the smoothing or weight function associated with \mathbf{x}_k . The following piecewise constant weight function is generally used in the smoothed FEM formulation,

$$W(\mathbf{x}_k - \mathbf{x}) = \begin{cases} 1/A_k^s & \mathbf{x} \in \Omega_k^s \\ 0 & \mathbf{x} \notin \Omega_k^s \end{cases} \quad (15)$$

where A_k^s is the area of the smoothing cell Ω_k^s . Substituting equation (15) into equation (14), one can obtain the smoothed strain by application of the Green's theorem

$$\bar{\boldsymbol{\varepsilon}}(\mathbf{x}_k) = \frac{1}{A_k^s} \int_{\Gamma_k^s} \mathbf{L}_k(\mathbf{x}) \cdot \mathbf{u}(\mathbf{x}) d\Gamma \quad (16)$$

where $\mathbf{L}_k(\mathbf{x})$ is a matrix function of the outward normal vector on the boundary Γ_k^s of

smoothing cell Ω_k^s and has the form

$$\mathbf{L}_k(\mathbf{x}) = \begin{bmatrix} n_x & 0 \\ 0 & n_y \\ n_y & n_x \end{bmatrix} \quad (17)$$

In such a way, the domain integration over Ω_k^s becomes a boundary integration along the edges of the smoothing cells. An isoparametric mapping is not necessary and the evaluation of the Jacobian in each element can be avoided. Also, we can see that the displacement gradient does not appear in equation (16). As a result, the derivatives of the shape functions are not required in the smoothed finite element method.

4.2 Extended finite element discretization

For a coherent interface, the displacement is assumed to be continuous across the interface. The strain field, however, may not be continuous, which is commonly called *weak discontinuity*. In the standard finite element formulation, the element edges are required to coincide with the geometrical interfaces to guarantee the accuracy and optimal convergence. In contrast, XFEM allows the mesh to be almost independent of interfaces by introducing additional enrichment, so that an inhomogeneity can be modeled by simply modifying the level set function without remeshing when its geometry changes. The displacement can be approximated in the following way [20]

$$\mathbf{u}^h(\mathbf{x}) = \mathbf{N}(\mathbf{x})\mathbf{d} + \mathbf{N}_a(\mathbf{x})\mathbf{a} \quad (18)$$

where \mathbf{d} and \mathbf{a} correspond to the nodal displacement vector and additional degrees of freedom due to enrichment, respectively, and $\mathbf{N}(\mathbf{x})$ and $\mathbf{N}_a(\mathbf{x})$ are the standard and enrichment shape function matrices

$$\mathbf{N}(\mathbf{x}) = [\mathbf{N}_1 \quad \mathbf{N}_2 \quad \cdots \quad \mathbf{N}_M], \quad \mathbf{N}_a(\mathbf{x}) = F(\mathbf{x})\mathbf{N} \quad (19)$$

where

$$\mathbf{N}_I = \begin{bmatrix} N_I & 0 \\ 0 & N_I \end{bmatrix} \quad (20)$$

The enrichment function $F(\mathbf{x})$ is given as suggested by [38]

$$F(\mathbf{x}) = \sum_{I=1}^M N_I(\mathbf{x})|\phi_I| - \left| \sum_{I=1}^M N_I(\mathbf{x})\phi_I \right| \quad (21)$$

Note that the enrichment function is zero in the elements that do not contain any part of the interface, so there are no spurious terms in the blending elements as shown in Figure 3 [38].

Substituting equation (18) into (16), the corresponding smoothing strain can be readily obtained in the following matrix form

$$\bar{\boldsymbol{\varepsilon}} = \bar{\mathbf{B}}\mathbf{d} + \bar{\mathbf{B}}_a\mathbf{a} \quad (22)$$

where

$$\bar{\mathbf{B}} = \frac{1}{A_k^s} \int_{\Gamma_k^s} \mathbf{L}_n(\mathbf{x})\mathbf{N}(\mathbf{x})d\Gamma, \quad \bar{\mathbf{B}}_a = \frac{1}{A_k^s} \int_{\Gamma_k^s} \mathbf{L}_n(\mathbf{x})\mathbf{N}_a(\mathbf{x})d\Gamma \quad (23)$$

On substituting displacement approximation (18) and smoothing strain (22) into the weak form, equations (8) and (9), a discrete linear system of equations can be easily obtained.

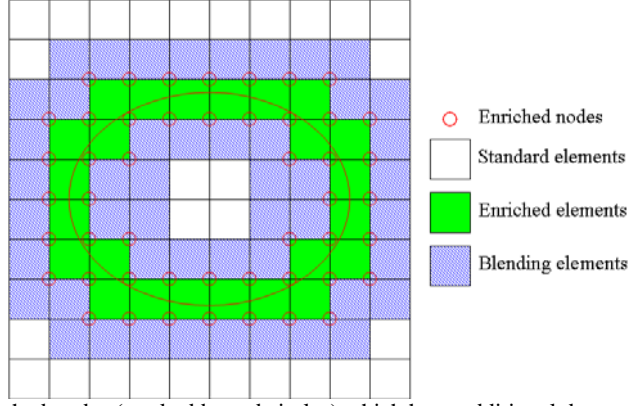


Figure 3. Enriched nodes (marked by red circles) which have additional degrees of freedom due to enrichment; enriched elements (marked by green squares) cut by the interface whose nodes are all enriched; blending elements (marked by shading squares) in which only part of the nodes are enriched.

4.3 Wachspress shape functions and smoothing cell partition

In the original paper on the smoothed FEM [29], non-mapped Lagrange shape functions are used to calculate the shape function values within a smoothed finite element, but the values at the vertices and mid-points of cell edges are evaluated using linear interpolations. This numerical scheme is valid only when the shape function is linear along the cell edges [39]. Unfortunately, this is not always the case. When the shape function is not linear along the edges in higher order elements or enriched elements in XFEM whose enrichment functions are not linear, the average shape function approximation and numerical integration scheme are not accurate. Bordas and Natarajan [39] suggested that the Wachspress interpolation can be used to retain the desirable features in the conventional smoothed FEM.

Following their ideas, we for the first time introduce the Wachspress shape functions into the SmXFEM framework to facilitate the accurate numerical integrals in the enriched finite elements. In this way, the shape function values at every edge of the smoothing cells can be directly obtained without any approximation. Moreover, since the Wachspress interpolants may be constructed on elements with arbitrary (including curved) edges, this makes our formulation general and attractive for curved interfaces. It is further shown that the numerical accuracy depends on the smoothing cell division used in the SmXFEM.

Although the Wachspress interpolants can be built for arbitrary n -sided polygonal elements with arbitrary edges, only quadrilateral elements shown in Figure 4 are formulated in the present work. Let $l_i(x, y) = 0$ be the function defining the line associated with the i -th edge of element Ω_e which can be uniquely written with coefficients a_i , b_i and c_i in the form,

$$l_i(x, y) = c_i - a_i x - b_i y \quad \text{for } (x, y) \in \Omega_e \Rightarrow l_i(x, y) > 0 \quad . \quad (24)$$

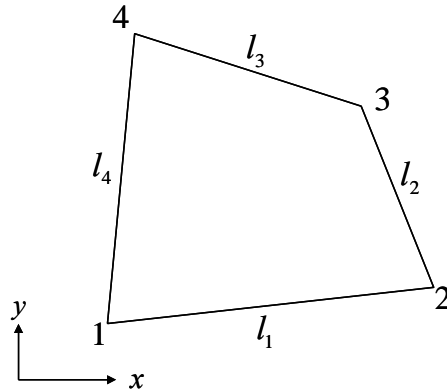


Figure 4. A sample quadrilateral element

The wedge function $w_I(x, y) = 0$ corresponding to the I -th node is defined by the following product if the two edges do not pass through node I

$$w_I(x, y) = \kappa_I l_{I+1}(x, y) l_{I+2}(x, y) \quad (25)$$

where κ_I are scalar constants. A compact definition of the **Wachspress shape function** corresponding to the I -th node is given by

$$N_I(x, y) = \frac{w_I(x, y)}{\sum_J w_J(x, y)} \quad (26)$$

In this definition, a necessary requirement for the shape function is to be linear along the element boundary, which can be achieved by an appropriate selection of constants κ_I as described by [40].

It should be noted that the shape function in (26) is not always linear within the element, nor are the Lagrange shape functions used in the original smoothed FEM [29] because of the bilinear term ‘ xy ’ in the basis. In the standard finite elements, an element can be divided into appropriate quadrilateral smoothing cells to avoid the nonlinearity of shape functions along the cell edges. In XFEM, however, the elements are generally cut by discontinuous interface with irregular geometries. This can be illustrated in Figure 5, in which a triangulation scheme used in standard XFEM is adopted to build the smoothing cells and the values of the shape function are plotted along the edges of smoothing cells. It is clearly seen that neither the standard nor the enriched shape functions are linear along the edges of smoothing cells in an enriched element. In these cases, integration of both the standard and the enrichment shape functions should be treated carefully to maintain accuracy and convergence rates. In this work, we will use three Gauss points in the enriched elements. In the standard elements, one Gauss point is enough to calculate the contour integral along each edge due to the linearity of the shape functions.

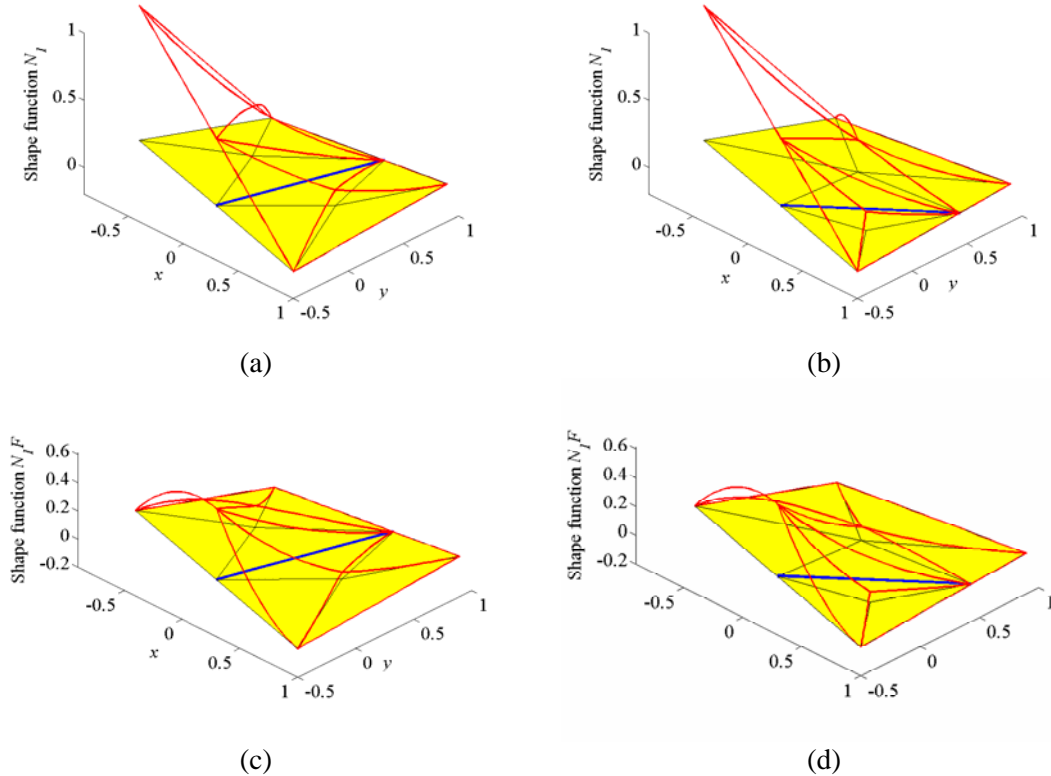


Figure 5. Triangular smoothing cell subdivision and shape functions along the edges of smoothing cells in an

enriched element. (a) and (b): standard shape functions; (c) and (d): enriched shape functions. The blue bold lines represent the interfaces.

To evaluate the strain matrix, an element needs to be further partitioned into smoothing cells. It has been pointed out that when the number of smoothing cells in the element approaches infinity, the smoothed FEM solution will approach the standard FEM solution [41]. In our SmXFEM, we devised a new partition scheme of smoothing cells for the enriched elements.

For the quadrilateral elements, an element is firstly divided into $m \times n$ quadrilateral smoothing cells, where m and n are the number of subcells in the x - and y - directions, respectively. In the enriched elements, those smoothing cells are further distinguished as standard smoothing cells and enriched smoothing cells. Then the enriched smoothing cells are partitioned into a group of sub-triangles. This scheme is illustrated in Figure 6.

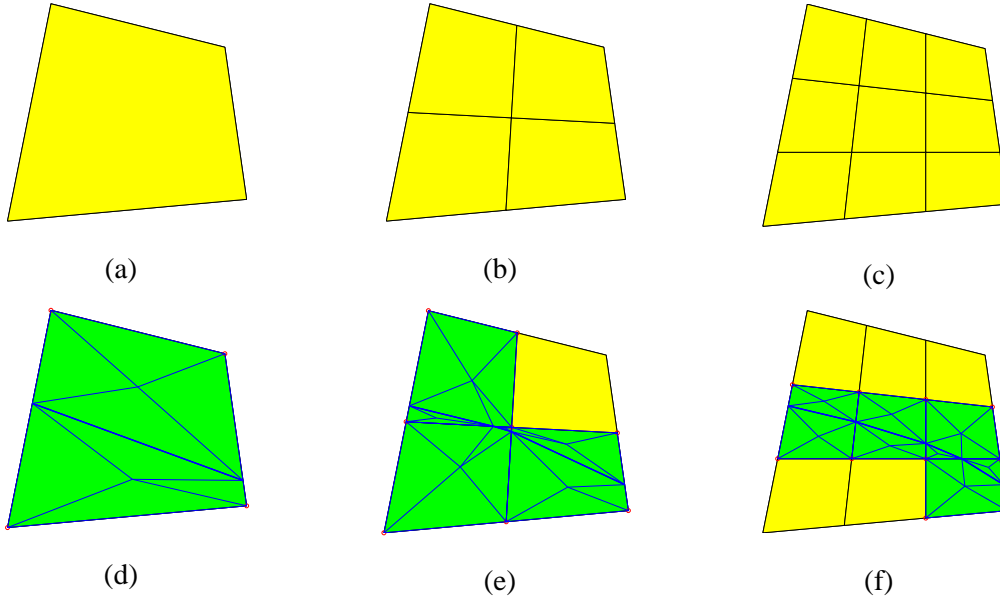


Figure 6. Partition of smoothing cells in an element. For the standard element: (a) 1×1 cell partition; (b) 2×2 cell partition; (c) 3×3 cell partition; For the enriched elements: (d) 1×1 cell partition; (e) 2×2 cell partition; (f) 3×3 cell partition. The yellow cells are standard smoothing cells and the green cells represent enriched smoothing cells.

It can be seen that the present partition scheme of smoothing cells provides great flexibility for arbitrary $m \times n$ cells partition according to the requirement of numerical accuracy and it is also extensible to higher order elements and three dimensional hexahedral elements. Another advantage of this scheme is that the curved interface can be more accurately resolved when the number of smoothing cells increases, which can be clearly seen in Figure 6(d)-(f).

5. Numerical examples

The SmXFEM developed above is suitable for a variety of problems dealing with nanoscale materials and structures with interface stress effects. In this paper, we focus on analyzing nano-inhomogeneities and their equilibrium shapes.

5.1 Convergence and computational efficiency

Consider an isotropic circular inclusion with a coherent interface embedded in an isotropic elastic matrix of infinite extent, subjected to a dilatational eigenstrain $\boldsymbol{\varepsilon}^* = \varepsilon^* \mathbf{I}$ as shown in Figure 7. The analytical solution to this problem is given by [5]. The bulk elastic constants for aluminum are $\lambda = 58.17$ GPa, $\mu = 26.13$ GPa [42] and the interface elastic constants are set as $\tau^S = -1$ N/m and $L^S = 10$ N/m [11]. The radius of the inclusion is taken as $R = 5$ nm. The

eigenstrain $\varepsilon^* = 0.01$ is used. The simulation is performed in a square domain of 15×15 nm and the boundary conditions are applied by imposing the exact displacements on the external boundary of the domain.

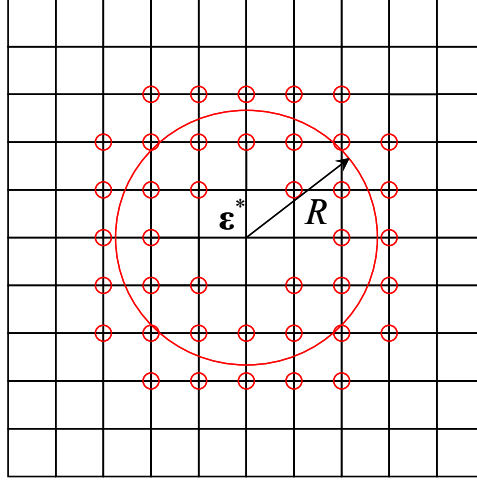


Figure 7. Computational model in smoothed XFEM with mesh, interface and enriched nodes.

In order to study the convergence of the present method, we define the following two norms, i.e. displacement norm e_d and energy norm e_e ,

$$e_d = \frac{\|\mathbf{u}^h - \mathbf{u}^{exact}\|}{\|\mathbf{u}^{exact}\|} \quad (27)$$

$$e_e = \sqrt{\frac{\int_{\Omega} (\boldsymbol{\varepsilon}^h(\mathbf{x}) - \boldsymbol{\varepsilon}^{exact}(\mathbf{x})) : \mathbf{L} : (\boldsymbol{\varepsilon}^h(\mathbf{x}) - \boldsymbol{\varepsilon}^{exact}(\mathbf{x})) d\Omega}{\int_{\Omega} \boldsymbol{\varepsilon}^{exact}(\mathbf{x}) : \mathbf{L} : \boldsymbol{\varepsilon}^{exact}(\mathbf{x}) d\Omega}} \quad (28)$$

where \mathbf{u}^h and $\boldsymbol{\varepsilon}^h$ are the displacement and strain fields obtained from the present SmXFEM by using different element sizes h . The quantities with superscript ‘*exact*’ are the exact solutions.

Figure 8 and Figure 9 show the displacement and energy norms for the cases without and with the interface stress, respectively. We can see that the optimal convergence rates are obtained for both smoothed and standard XFEM when the interfacial energy effects are ignored. The convergence rate is suboptimal when interfacial energy effects are considered and nearly 0.88 for the energy norm except for the 1×1 cell subdivision. The convergence rate is however much higher than that of 0.4-0.5 reported in [27] for the conventional XFEM. It is seen that the SmXFEM shows better performance over the standard XFEM if more than 1×1 cells are used. This is more obvious in Figure 9 where the interfacial energy effects are considered. We can also find that the relative errors decrease with the increase of the number of smoothing cells. However, when the number of smoothing cells exceeds 2×2 , the improvement of the accuracy is not very significant.

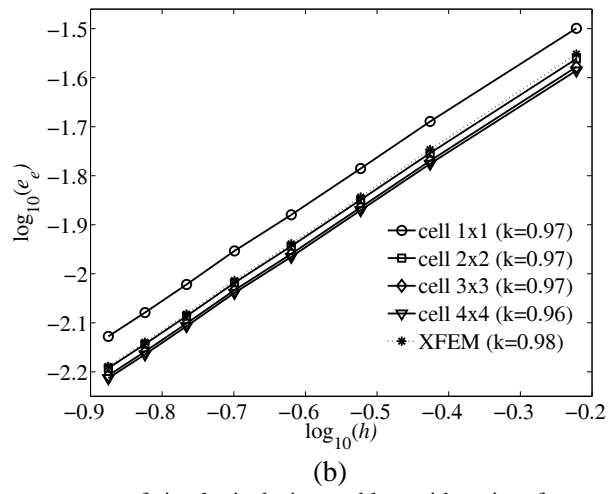
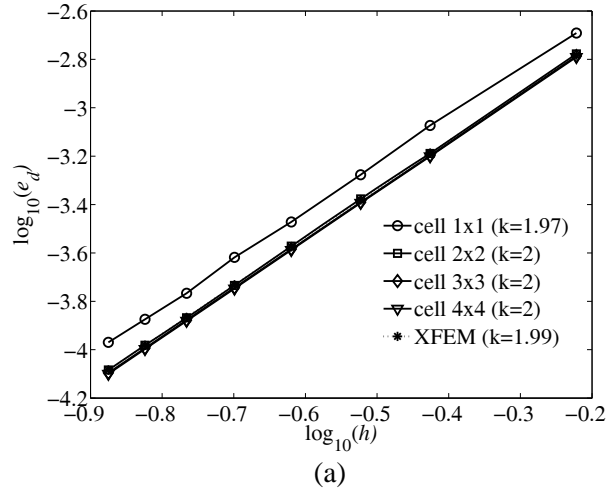
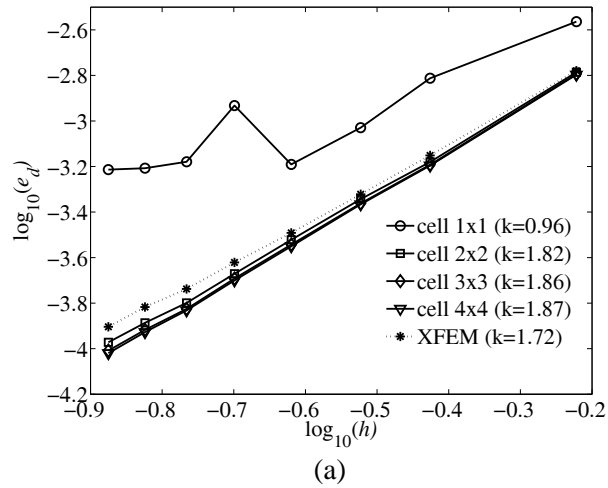


Figure 8. Convergence rate of circular inclusion problem without interface stress. (a) Displacement norm; (b) Energy norm.



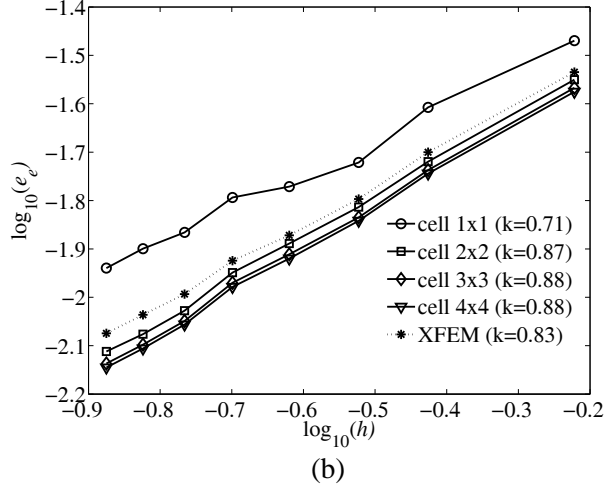


Figure 9. Convergence rate of circular inclusion problem with interface stress. (a) Displacement norm; (b) Energy norm.

As we mentioned, in the SmXFEM, the evaluation of the derivatives of shape functions and the Jacobian matrix in each element is not required to calculate the strain matrix. Moreover, the domain integrals are transformed into boundary integrals. In addition, in the standard XFEM, the numerical quadrature has to be performed over all the subtriangles in an enriched element. Therefore, two isoparametric mapping steps are required: mapping from the reference coordinate ξ_{Δ} of subtriangles to the global coordinate \mathbf{x} and an inverse map from the global to reference coordinate system of the bi-unit square $\xi_{\square} = \mathbf{x}^{-1}(\xi_{\square})$. Generally iterative algorithms are required for the second step mapping [33], which would be time consuming in the standard XFEM when the elements cut by the interface are numerous. However, the Wachspress shape function in our SmXFEM is defined directly on the global coordinate system without requiring any inverse coordinate mapping. Those characteristics can effectively reduce the computational cost.

Figure 10 compares the computational time versus total element numbers for the SmXFEM and the standard XFEM. The program runs on Windows XP operating system with Intel Xeon CPU 2.27 GHz. Since the only difference between XFEM and SmXFEM is the way to calculate the element stiffness matrix, we use the total time consumed to form the global matrix as the efficiency measure. It is clearly seen that the slope for SmXFEM is close to 1, which implies that the computational time is linearly proportional to the total number of elements. For XFEM, this slope is nearly 1.86, which means that the computational cost increases exponentially with the number of elements. This advantage makes SmXFEM attractive for large scale computations. Moreover, for some time dependent problems involving moving interfaces, the elastic field must be calculated at each time step to evaluate the interface velocity. In these cases, the computational expenses are typically significant, even for 2D problems and the proposed method can hence prove advantageous. The numerical examples will be given in sec. 5.3.

Furthermore, to balance the computational cost and accuracy, we can flexibly choose different combination of cell partition schemes, such as 2×2 cells in the standard elements and 4×4 cells in the enriched elements, which will be used in the following numerical examples.

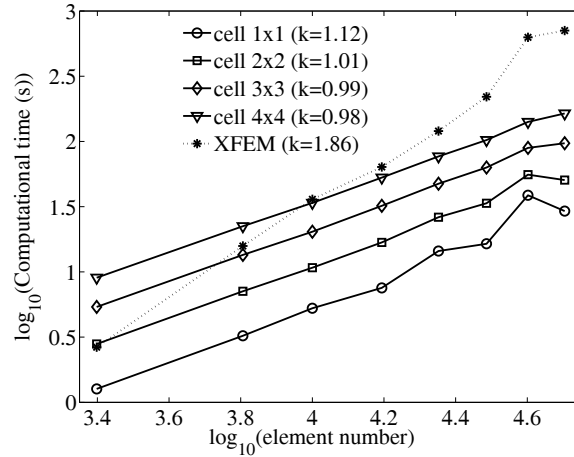
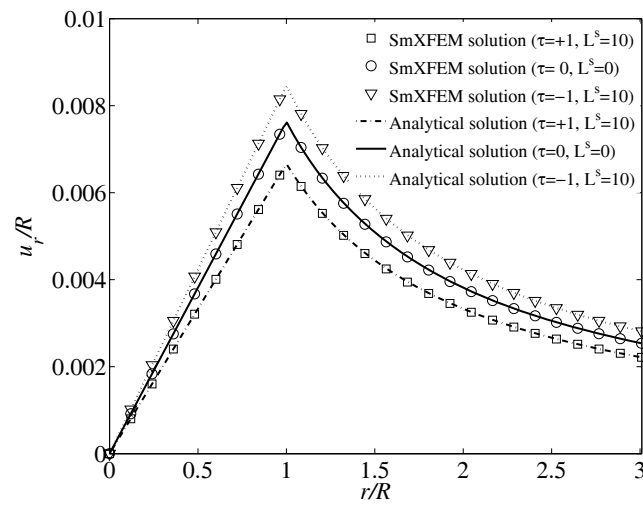


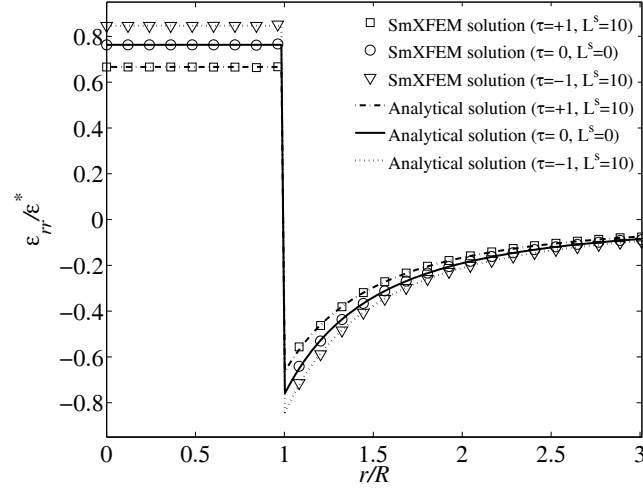
Figure 10. Computational time vs. element number.

5.2 Elastic field of a nano-inclusion with interface effects

The elastic field of the nano-inclusion problem described in section 5.1 is considered here. A regular mesh with 50×50 quadrilateral elements. The displacement and strain components in the radial direction with and without interface effects are compared and given in Figure 11. It is clearly seen that the present SmXFEM results are in very good agreement with the exact solutions, and capable of accurately capturing the interface effects. This again provides us with confidence on the validity of the approach to explore more complex problems.



(a)



(b)

Figure 11. Comparison of the normalized radial displacement u_r (a) and strain ϵ_{rr} (b) from the exact and the present SmXFEM solutions.

5.3 Equilibrium shapes of nano-particles in elastic solids

It has been experimentally observed that particles (precipitates) in nickel based superalloys may evolve, with increasing particle size, from an initially spherical shape to a cuboidal shape with flat edges and round corners [43, 44]. Most theoretical considerations are based on the assumption that the equilibrium morphology of such particles is governed by minimizing the total system energy. For example, Kaganova and Roitburd [45], Johnson and coworkers [46, 47] analyzed the shape transitions of precipitate particles in an infinite elastic matrix. The equilibrium shape and morphological development of misfit particles were also formulated based on boundary integral methods, in which a set of marker particles are placed on the phase interface to track the moving boundaries [48-50].

In this section, we will apply the proposed hybrid smoothed XFEM/level set method to predict the equilibrium shapes of misfit particles in an elastically anisotropic system. The SmXFEM is used to compute the elastic field and evaluate interface velocity, and the level set method is used to implicitly describe and update the geometry of the material interface. We assume that the total system energy is the sum of the elastic strain energy due to the misfit strain and the interfacial energy, so that the problem is equivalent to finding a set of discrete values (at the nodes) of level set that minimizes the total system energy Π under the constant volume constraint.

In the absence of body force and external loading, the augmented energy functional can be modified by incorporating a Lagrange multiplier λ :

$$L = \Pi + \lambda(V_\Omega - V_0) = U^b + U^s + \lambda \left(\int_\Omega dV - V_0 \right) \quad (29)$$

The variation of this Lagrange functional (see Mueller et al. [49] and Kolling and Gross [51] for details) yields

$$\delta L = - \int_\Gamma (G_n - \lambda) \delta n dS + \delta \lambda \left(\int_\Omega dV - V_0 \right) \quad (30)$$

where δn represents a shape variation of the interface in the normal direction and

$$G_n = \mathbf{n} \cdot \llbracket \boldsymbol{\Sigma} \rrbracket \cdot \mathbf{n} + \gamma \kappa \quad (31)$$

Here $\llbracket \cdot \rrbracket$ denotes the quantity jump across the interface. $\boldsymbol{\Sigma} = w\mathbf{I} - \boldsymbol{\sigma} \cdot \nabla \mathbf{u}$ is the Eshelby

energy momentum tensor where w denotes the elastic energy density, κ represents the interfacial mean curvature. The Lagrange multiplier is

$$\lambda = \frac{\int_{\Gamma} G_n dS}{\int_{\Gamma} dS} \quad (32)$$

Next, we take the shape variation of the interface δn as the normal velocity of level set at the interface, i.e. $v_n = \delta n$ and consider the volume conservation condition $\int_{\Omega} dV = V_0$.

Then the energy functional (30) becomes

$$\delta L = -\int_{\Gamma} (G_n - \lambda) v_n dS \quad (33)$$

Note that if we take

$$v_n = G_n - \lambda = \mathbf{n} \cdot \llbracket \boldsymbol{\Sigma} \rrbracket \cdot \mathbf{n} + \gamma \kappa - \lambda \quad (34)$$

at the interface, we obtain

$$\delta L = -\int_{\Gamma} v_n^2 dS \leq 0 \quad (35)$$

which implies that the total system energy will keep decreasing during the interface evolution until the interface velocity goes to zero.

It is noted that the velocity field in the level set equation is defined in the spatial domain, but the velocity given in (34) is only defined on the interface. In the following example, a second order fast marching method [52] is used to extend the interface velocity to the entire computational domain, and the third order accurate Hamilton-Jacobi WENO finite difference spatial discretization and third order TVD Runge-Kutta (RK) time discretization schemes are used to solve the hyperbolic level set equation [53].

We use the anisotropic elastic constants of Ni for the matrix, which are $C_{11}^M = 246.5$ GPa, $C_{12}^M = 147.3$ GPa and $C_{44}^M = 124.7$ GPa in Voigt notation. We adopt the assumption that the elastic constants of particles are proportional to that of matrix, $C_{ij}^I = \alpha C_{ij}^M$ [54], so that we have hard particles when $\alpha > 1$, soft particles when $\alpha < 1$ and homogeneous particles when $\alpha = 1$. For simplicity, we further assume the interfacial energy is constant that $\gamma = \gamma_0$, where $\gamma_0 = 20$ ergs cm⁻² and the dilatational misfit eigenstrain $\varepsilon^* = 0.3\%$ [55]. Therefore, we can introduce the dimensionless characteristic length $L = C_{44}^I \varepsilon_0^2 R_0 / \gamma$, in which R_0 is the effective radius of particle, for example, $R_0 = \sqrt{A_0 / \pi}$ where A_0 is the area of a particle in two-dimensions. It can be clearly seen that the interfacial energy plays an important role when L is small, while the elastic bulk energy becomes more important when L increases. In the following numerical examples, we further assume that the initial shapes of the particles are circles for each case and the material axis <100> directions are the same as the coordinate directions.

Figure 12 shows the equilibrium shapes of an isolated particle at different sizes and stiffness ratios. It is seen that for the hard and homogeneous particles that $\alpha \geq 1$, the equilibrium morphologies undergo a transition from the circle-like to the square-like shapes with round corners when the particle size increases. This is in good agreement with experimental observations [43]. For the soft particles, the cuboidal shape remains for $L = 5$. However, the equilibrium shape gradually becomes concave with the increase of the particle size as shown in the uppermost row of Figure 12.

$L = 5$

$L = 10$

$L = 20$

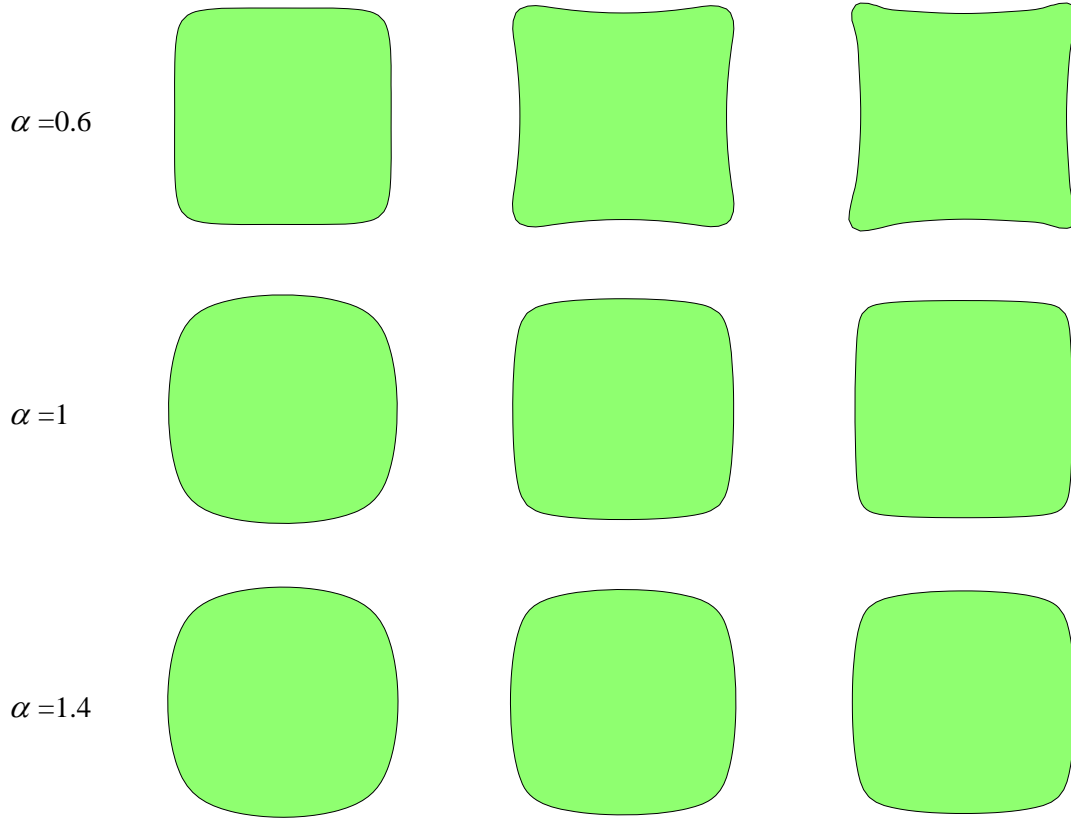


Figure 12. Equilibrium shapes of an isolated inhomogeneity for $\alpha = 0.6, 1, 1.4$ and $L = 5, 10, 20$.

It should be mentioned that the present results are very similar to that obtained from boundary integral methods [54, 56] and finite element methods [57], in which a number of marker points have to be placed on the geometric interface to track its motion. However, the proposed hybrid SmXFEM/LSM approach inherits the merits of both the extended finite element and level set method and provides distinct advantages to model the moving interface in solid materials. The main advantage of the (smoothed) XFEM is that the meshes do not have to conform to the evolving interfaces, so that no remeshing is required during the evolution. In addition, the computational cost for evaluating the elastic field at each time step is effectively reduced. The implicit description of moving interfaces using the level set method naturally allows topological changes of phase boundaries, which are generally very hard to handle in the conventional marker particle method.

6. Conclusion

In this paper, we developed a hybrid smoothed extended finite element/level set method with evolving interfaces for modeling equilibrium shapes of nano-inhomogeneities. A linear interface elasticity model was adopted to account for effects of interfacial excess energy. It is shown that once the interfacial energy is considered, the energetically favorable shapes of precipitate particles would depend on the particle size, misfit strain and the elastic constants of bulk materials due to the competition between the interfacial energy and anisotropic elastic energy. The SmXFEM developed here has several advantages over the conventional XFEM methods. For example, the Jacobian matrix and the derivatives of the standard and enrichment shape functions need not be computed and the domain integrals in the finite elements are replaced by boundary integrals, which can efficiently reduce the computational cost without loss of accuracy. The Wachspress shape functions are for the first time introduced into the SmXFEM framework, which greatly facilitates accurate numerical integration along the edges of smoothing cells. The accuracy and convergence rates are studied in the numerical results, which show superior to the standard XFEM [27]. Further, we showed that the computational

time of our SmXFEM scales linearly with the number of elements, while that of our implementation of the XFEM increases exponentially (exponent 1.86) with the number of elements. We believe that the hybrid SmXFEM/LSM developed here is an effective numerical tool for nano-scale material analysis and designs, and can be used to study nano-scale inhomogeneous materials and structures with complex morphological changes. Future works includes extension to realistic three-dimensional cases and the coupling with model reduction techniques for highly non-linear problems [58].

Acknowledgement

XZ and JQ acknowledge the partial support by NSF through CMMI-1200075. SPAB acknowledges partial support from the European Research Council Starting Independent Research Grant (ERC Stg No. 279578) and EPSRC's grants EP/G042705/1 and [EP/I006761/1](#).

Reference:

1. Gurtin ME and Murdoch AI (1975) Continuum Theory of Elastic-Material Surfaces. Archive for Rational Mechanics and Analysis 57: 291-323 DOI:10.1007/BF00261375
2. Gurtin ME, Weissmuller J and Larche F (1998) A general theory of curved deformable interfaces in solids at equilibrium. Philos Mag A 78: 1093-1109 DOI:10.1080/01418619808239977
3. Duan HL, Wang J, Huang ZP and Karimhaloo BL (2005) Size-dependent effective elastic constants of solids containing nano-inhomogeneities with interface stress. J Mech Phys Solids 53: 1574-1596 DOI:10.1016/j.jmps.2005.02.009
4. Miller RE and Shenoy VB (2000) Size-dependent elastic properties of nanosized structural elements. Nanotechnology 11: 139-147 DOI:10.1088/0957-4484/11/3/301
5. Sharma P and Ganti S (2004) Size-dependent Eshelby's tensor for embedded nano-inclusions incorporating surface/interface energies. J Appl Mech-T Asme 71: 663-671 DOI:10.1115/1.1781177
6. Zhao XJ and Qu J (2012) Effects of interfacial excess energy on the elastic field of a nano-inhomogeneity. Mech Mater 55: 41-48 DOI:10.1016/j.mechmat.2012.07.008
7. Dingreville R, Qu JM and Cherkaoui M (2005) Surface free energy and its effect on the elastic behavior of nano-sized particles, wires and films. J Mech Phys Solids 53: 1827-1854 DOI:10.1016/j.jmps.2005.02.012
8. Zhao XJ and Rajapakse RKND (2009) Analytical solutions for a surface-loaded isotropic elastic layer with surface energy effects. Int J Eng Sci 47: 1433-1444 DOI: 10.1016/j.ijengsci.2008.12.013
9. Olsson PAT and Park HS (2012) On the importance of surface elastic contributions to the flexural rigidity of nanowires. J Mech Phys Solids 60: 2064-2083 DOI: 10.1016/j.jmps.2012.07.009
10. Gao W, Yu SW and Huang GY (2006) Finite element characterization of the size-dependent mechanical behaviour in nanosystems. Nanotechnology 17: 1118-1122 DOI: 10.1088/0957-4484/17/4/045
11. Tian L and Rajapakse RKND (2007) Finite element modelling of nanoscale inhomogeneities in an elastic matrix. Comp Mater Sci 41: 44-53 DOI:10.1016/j.commatsci.2007.02.013
12. She H and Wang BA (2009) A geometrically nonlinear finite element model of nanomaterials with consideration of surface effects. Finite Elements in Analysis and Design 45: 463-467 DOI:10.1016/j.finel.2009.01.002
13. Javili A and Steinmann P (2009) A finite element framework for continua with boundary energies. Part I: The two-dimensional case. Comput Method Appl M 198: 2198-2208 DOI:10.1016/j.cma.2009.02.008
14. Javili A and Steinmann P (2010) A finite element framework for continua with boundary energies. Part II: The three-dimensional case. Comput Method Appl M 199: 755-765 DOI: 10.1016/j.cma.2009.11.003
15. He J and Lilley CM (2009) The finite element absolute nodal coordinate formulation incorporated with surface stress effect to model elastic bending nanowires in large deformation. Comput Mech 44: 395-403 DOI:10.1007/s00466-009-0380-9
16. Yun G and Park HS (2008) A finite element formulation for nanoscale resonant mass sensing using the surface Cauchy-Born model. Comput Method Appl M 197: 3324-3336 DOI:10.1016/j.cma.2008.01.010
17. Park HS, Klein PA and Wagner GJ (2006) A surface Cauchy-Born model for nanoscale materials. Int J Numer Meth Eng 68: 1072-1095 DOI: 10.1002/nme.1754
18. Park HS and Klein PA (2007) Surface Cauchy-Born analysis of surface stress effects on metallic nanowires. Phys Rev B 75:10.1103/PhysRevB.75.085408

19. Moës N, Dolbow J and Belytschko T (1999) A finite element method for crack growth without remeshing. *Int J Numer Meth Eng* 46: 131-150 DOI: 10.1002/(SICI)1097-0207(19990910)46:1<131::AID-NME726>3.0.CO;2-J
20. Sukumar N, Chopp DL, Moes N and Belytschko T (2001) Modeling holes and inclusions by level sets in the extended finite-element method. *Comput Method Appl M* 190: 6183-6200 DOI:10.1016/S0045-7825(01)00215-8
21. Chessa J, Smolinski P and Belytschko T (2002) The extended finite element method (XFEM) for solidification problems. *Int J Numer Meth Eng* 53: 1959-1977 DOI: 10.1002/Nme.386
22. Chessa J and Belytschko T (2003) An extended finite element method for two-phase fluids. *J Appl Mech-T Asme* 70: 10-17 DOI: 10.1115/1.1526599
23. Duddu R, Bordas S, Chopp D and Moran B (2008) A combined extended finite element and level set method for biofilm growth. *Int J Numer Meth Eng* 74: 848-870 DOI: 10.1002/Nme.2200
24. Duddu R, Chopp DL and Moran B (2009) A Two-Dimensional Continuum Model of Biofilm Growth Incorporating Fluid Flow and Shear Stress Based Detachment. *Biotechnol Bioeng* 103: 92-104 DOI: 10.1002/Bit.22233
25. Fries TP and Belytschko T (2010) The extended/generalized finite element method: An overview of the method and its applications. *Int J Numer Meth Eng* 84: 253-304 DOI: 10.1002/Nme.2914
26. Bordas S, Nguyen PV, Dunant C, Guidoum A and Nguyen-Dang H (2007) An extended finite element library. *Int J Numer Meth Eng* 71: 703-732 DOI: 10.1002/Nme.1966
27. Yvonnet J, Le Quang H and He QC (2008) An XFEM/level set approach to modelling surface/interface effects and to computing the size-dependent effective properties of nanocomposites. *Comput Mech* 42: 119-131 DOI: 10.1007/s00466-008-0241-y
28. Farsad M, Vernerey FJ and Park HS (2010) An extended finite element/level set method to study surface effects on the mechanical behavior and properties of nanomaterials. *Int J Numer Meth Eng* 84: 1466-1489 DOI: 10.1002/Nme.2946
29. Liu GR, Dai KY and Nguyen TT (2007) A smoothed finite element method for mechanics problems. *Comput Mech* 39: 859-877 DOI: 10.1007/s00466-006-0075-4
30. Wachspress EL (1975) *A rational finite element basis* Academic Press, New York
31. Shuttleworth R (1950) The Surface Tension of Solids. *P Phys Soc Lond A* 63: 444-457 DOI:10.1088/0370-1298/63/5/302
32. Osher S and Sethian JA (1988) Fronts Propagating with Curvature-Dependent Speed - Algorithms Based on Hamilton-Jacobi Formulations. *J Comput Phys* 79: 12-49 DOI: 10.1016/0021-9991(88)90002-2
33. Sukumar N and Prevost JH (2003) Modeling quasi-static crack growth with the extended finite element method Part I: Computer implementation. *Int J Solids Struct* 40: 7513-7537 DOI: 10.1016/j.ijsolstr.2003.08.002
34. Moumnassi M, Belouettar S, Bechet E, Bordas SPA, Quoirin D and Potier-Ferry M (2011) Finite element analysis on implicitly defined domains: An accurate representation based on arbitrary parametric surfaces. *Comput Method Appl M* 200: 774-796 DOI: 10.1016/j.cma.2010.10.002
35. Gracie R, Oswald J and Belytschko T (2008) On a new extended finite element method for dislocations: Core enrichment and nonlinear formulation. *J Mech Phys Solids* 56: 200-214 DOI: 10.1016/j.jmps.2007.07.010
36. Legay A, Chessa J and Belytschko T (2006) An Eulerian-Lagrangian method for fluid-structure interaction based on level sets. *Comput Method Appl M* 195: 2070-2087

DOI:10.1016/j.cma.2005.02.025

37. Chen JS, Wu CT, Yoon S and You Y (2001) A stabilized conforming nodal integration for Galerkin mesh-free methods. *Int J Numer Meth Eng* 50: 435-466
DOI:10.1002/1097-0207(20010120)50:2<435::AID-NME32>3.0.CO;2-A
38. Moës N, Cloirec M, Cartraud P and Remacle JF (2003) A computational approach to handle complex microstructure geometries. *Comput Method Appl M* 192: 3163-3177 DOI: 10.1016/S0045-7825(03)00346-3
39. Bordas SPA and Natarajan S (2010) On the approximation in the smoothed finite element method (SFEM). *Int J Numer Meth Eng* 81: 660-670 DOI: 10.1002/Nme.2713
40. Dasgupta G (2003) Interpolants within convex polygons: Wachspress' shape functions. *J Aerospace Eng* 16: 1-8 DOI: 10.1061/(Asce)0893-1321(2003)16:1(1)
41. Liu GR, Nguyen TT, Dai KY and Lam KY (2007) Theoretical aspects of the smoothed finite element method (SFEM). *Int J Numer Meth Eng* 71: 902-930 DOI: 10.1002/Nme.1968
42. Meyers MA and Chawla KK (2009) *Mechanical behavior of materials*, 2nd edn. Cambridge University Press, Cambridge, UK ; New York
43. Fahrman M, Fratzi P, Paris O, Fahrman E and Johnson WC (1995) Influence of Coherency Stress on Microstructural Evolution in Model Ni-Al-Mo Alloys. *Acta Metall Mater* 43: 1007-1022 DOI:10.1016/0956-7151(94)00337-H
44. Maheshwari A and Ardell AJ (1993) Morphological Evolution of Coherent Misfitting Precipitates in Anisotropic Elastic Media. *Phys Rev Lett* 70: 2305-2308 DOI: 10.1103/PhysRevLett.70.2305
45. Kaganova IM and Roitburd AL (1988) Equilibrium between elastically interacting phases. *Soviet Physics - JETP* 67: 1173-1183 DOI
46. Johnson WC and Cahn JW (1984) Elastically Induced Shape Bifurcations of Inclusions. *Acta Metallurgica* 32: 1925-1933 DOI:10.1016/0001-6160(84)90174-3
47. Johnson WC, Berkenpas MB and Laughlin DE (1988) Precipitate Shape Transitions during Coarsening under Uniaxial-Stress. *Acta Metallurgica* 36: 3149-3162 DOI: 10.1016/0001-6160(88)90051-X
48. Schmidt I, Mueller R and Gross D (1998) The effect of elastic inhomogeneity on equilibrium and stability of a two particle morphology. *Mech Mater* 30: 181-196 DOI: 10.1016/S0167-6636(98)00047-7
49. Mueller R, Eckert S and Gross D (2000) 3D equilibrium shapes of periodically arranged anisotropic precipitates with elastic misfit. *Archive of Applied Mechanics* 52: 663-683 DOI
50. Voorhees PW, Mcfadden GB and Johnson WC (1992) On the Morphological Development of second-Phase Particles in Elastically-Stressed Solids. *Acta Metall Mater* 40: 2979-2992 DOI: 10.1016/0956-7151(92)90462-N
51. Kolling S, Mueller R and Gross D (2003) The influence of elastic constants on the shape of an inclusion. *Int J Solids Struct* 40: 4399-4416 DOI: 10.1016/S0020-7683(03)00183-5
52. Sethian JA (1999) Fast marching methods. *Siam Rev* 41: 199-235 DOI: 10.1137/S0036144598347059
53. Osher S and Fedkiw RP (2003) *Level set methods and dynamic implicit surfaces* Springer, New York
54. Schmidt I and Gross D (1997) The equilibrium shape of an elastically inhomogeneous inclusion. *J Mech Phys Solids* 45: 1521-1549 DOI: 10.1016/S0022-5096(97)00011-2
55. Su CH and Voorhees PW (1996) *The dynamics of precipitate evolution in elastically stressed*

- solids .1. Inverse coarsening. *Acta Mater* 44: 1987-1999 DOI: 10.1016/1359-6454(95)00284-7
56. Thompson ME, Su CS and Voorhees PW (1994) The Equilibrium Shape of a Misfitting Precipitate. *Acta Metall Mater* 42: 2107-2122 DOI: 10.1016/0956-7151(94)90036-1
57. Jog CS, Sankarasubramanian R and Abinandanan TA (2000) Symmetry-breaking transitions in equilibrium shapes of coherent precipitates. *J Mech Phys Solids* 48: 2363-2389 DOI: 10.1016/S0022-5096(00)00005-3
58. Kerfriden P, Gosselet P, Adhikari S and Bordas SPA (2011) Bridging proper orthogonal decomposition methods and augmented Newton-Krylov algorithms: An adaptive model order reduction for highly nonlinear mechanical problems. *Comput Method Appl M* 200: 850-866 DOI: 10.1016/j.cma.2010.10.009